Faraday Discussions

Cite this: *Faraday Discuss.*, 2014, **173**, 215

PAPER

Nitrogen segregation in nanocarbons

C. P. Ewels,*[a] D. Erbahar,[ab] Ph. Wagner,[a] X. Rocquefelte,[a] R. Arenal,[cd] P. Pochet,[e] M. Rayson,[f] M. Scardamaglia,[h] C. Bittencourt[h] and P. Briddon[ag]

Received 16th May 2014, Accepted 13th June 2014
DOI: 10.1039/c4fd00111g

We explore the behaviour of nitrogen doping in carbon nanomaterials, notably graphene, nanotubes, and carbon thin films. This is initially *via* a brief review of the literature, followed by a series of atomistic density functional calculations. We show that at low concentrations, substitutional nitrogen doping in the sp^2-C graphenic basal plane is favoured, however once the nitrogen concentration reaches a critical threshold there is a transition towards the formation of the more thermodynamically-favoured nitrogen terminated 'zigzag' type edges. These can occur either *via* formation of finite patches (polycyclic aromatic azacarbons), strips of sp^2 carbon with zigzag nitrogen edges, or internal nitrogen-terminated hole edges within graphenic planes. This transition to edge formation is especially favoured when the nitrogen can be partially functionalised with, *e.g.* hydrogen. By comparison with available literature results, notably from electron energy loss spectroscopy and X-ray spectroscopy, the current results suggest that much of the nitrogen believed to be incorporated into carbon nanoobjects is instead likely to be present terminating the edges of carbonaceous impurities attached to nanoobject's surface. By comparison to nitrogen-doped tetrahedrally amorphous carbon, we suggest that this transition at around 10–20% nitrogen concentration and above towards sp^2 coordination *via* internal nitrogen-terminated edge formation may be a general property of nitrogen-doped carbon materials.

[a]*IMN, CNRS UMR6502, Universit de Nantes, 44300 Nantes, France. E-mail: chris.ewels@cnrs-imn.fr; Tel: +33 (0)2 40 37 64 07*

[b]*Physics Department, Gebze Institute of Technology, Gebze, Kocaeli 41400, Turkey*

[c]*Laboratorio de Microscopias Avanzadas (LMA), Instituto de Nanociencia de Aragon (INA), Universidad de Zaragoza, Calle Mariano Esquillor, 50018 Zaragoza, Spain*

[d]*Fundacion ARAID, 50018 Zaragoza, Spain*

[e]*Univ. Grenoble Alpes, INAC-SP2M, L Sim and CEA, INAC-SP2M, Atomistic Simulation Lab., F-38000 Grenoble, France*

[f]*Department of Chemistry, University of Surrey, Guildford, Surrey, UK*

[g]*School of Natural Sciences, University of Newcastle upon Tyne, Newcastle upon Tyne, UK*

[h]*Chemistry of Interaction Plasma Surface (ChIPS), University of Mons, Belgium*

1 Introduction

Heteroatom doping has long been of interest as a way to modify the physical, chemical and electronic properties of carbon materials.[1–5] With its five valence electrons compared to carbon's four, and very similar atomic radius, nitrogen is a natural choice for doping nanocarbons.[5–8] Nitrogen doping of carbon nanomaterials has been explored as a way to electronically dope carbon, chemically activate the carbon surface and change solubility, and improve the electrical and thermal conductivity of carbon nanotubes (CNTs)[9–13] with the resulting materials showing promise for oxygen reduction reactions[14,15] energy-storage,[16,17] gas[18] and bio[19] sensors, and in the synthesis of 3D macrostructures.[20]

Nitrogen-doped single walled nanotubes (SWNTs) generally exhibit morphologies similar to their undoped counterparts, namely straight non-buckled nanotube walls.[21,22] However nitrogen-doped multi-walled nanotubes (MWNTs) exhibit very distinct morphologies, significantly different from their undoped counterparts. These tubes always have a so-called "bamboo" structure, where the nanotube contains a regularly spaced array of internal carbon walls, or 'herringbone' structures where the tubes are constructed from a stacked-cone carbon arrangement. Nitrogen-doped nanotubes are less stable than their pure carbon counterparts, breaking easily under the electron beam in the transmission electron microscope (TEM)[23,24] and oxidising at lower temperatures than undoped tubes.[25] Similar behavior under the electron beam has also been observed in N-doped graphene compared to pristine graphene.[23,26]

Nitrogen doping in nanocarbons exhibits similar spectral signatures whether in graphene,[27,28] nitrogen-doped carbon thin films,[29] SWNTs[23,30] (see Fig. 1) or nanodiamonds.[31] The nitrogen N1 is seen to split into two distinct peaks at $\approx$398 and 402 eV, with a third intermediate peak at $\sim$400 eV seen in MWNTs.[27,32] The peak at $\sim$398 eV is commonly associated with pyridinic nitrogen, defined as a nitrogen atom with two aromatic carbon neighbours. This can occur next to a vacancy, or at an edge site, for example at an open nanotube tip[7] (see Fig. 2). The peak at $\sim$400 eV is commonly assigned to pyrrolic nitrogen,[32,33] substitutional nitrogen atoms in a region of defective non-aromatic lattice (such as neighbouring pentagons and/or heptagons)[24] or sp cyanide (triple bonded to carbon).[34,35] Finally the peak at $\sim$401–402 eV is normally assigned to substitutional (graphitic) nitrogen.[36]

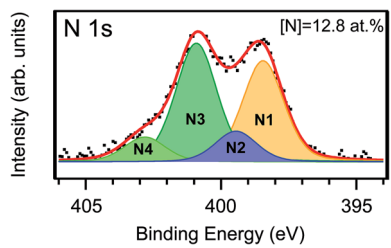

Fig. 1 N1s core level spectra from nitrogen implanted CVD few-layer graphene; experimental data (dotted line), peaks resulting from a least-square fitting procedure (continuous red line). A Shirley-type background was subtracted (adapted from ref. 27).

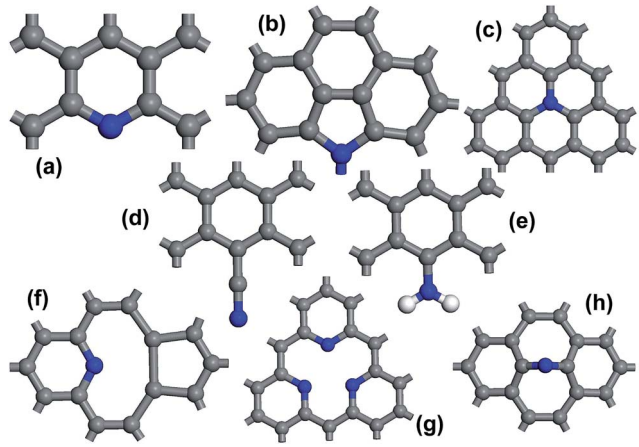

Fig. 2 Possible bonding configurations for N in graphitic networks, (a) pyridinic-like N, (b) pyrrolic-type nitrogen (other pyrrolic configurations are possible provided the nitrogen remains sp^3 coordinated), (c) graphitic substitutional nitrogen, (d) Nitrile $-C{\equiv}N$, (e) $-NH_2$, (f) pyridinic N-vacancy complex, (g) pyridinic N_3-vacancy, (h) interstitial nitrogen. Reproduced from ref. 7.

Other macroscopic spectroscopic techniques as Raman spectroscopy have also been successfully employed for the study of doped sp^2-carbon nanomaterials.[37,38] In N-doped SWNTs, the shift and broadening of characteristic Raman peaks provides information about the doping degree of these materials.[39,40] We focus in this current article on X-ray and electron spectroscopy results.

2 Substitutional nitrogen in bilayer graphene

The current investigation was initiated by the fact that experiments seem to suggest fundamental limits to nitrogen doping concentrations in CNTs. In SWNTs concentrations appear limited to ~1% at most,[23,24,30] whereas in MWNTs average concentrations can reach up to ~15–20%.[41,42] While local concentrations can reach 25–30%,[43] it has been shown with electron tomography that the nitrogen is not homogeneously distributed in this case and instead the sample contains nitrogen-rich non-graphitic regions.[42] To determine a theoretical maximum attainable upper limit for nitrogen substitution in an sp^2-layered carbon system, we performed a series of density functional calculations.

We constructed supercells containing AB-bilayer graphene (see Computational method below), then substituted random carbon atoms with nitrogen, imposing the rule that neighbouring atoms could not be substituted. The systems were then fully geometrically optimized. This process was repeated for a number of different nitrogen configurations, at a range of different nitrogen concentrations from 0–50%. Substituting carbon with nitrogen disrupts the surrounding electronic π-cloud, and at a certain point the surrounding carbon atoms are no longer stable in an sp^2 configuration, and instead have a tendency to cross-link with the neighbouring layer forming sp^3-bonded carbon. The natural limit of this is at 50% nitrogen incorporation, at which point every other carbon atom has been nitrogen substituted. The remaining carbon atoms all cross-link between the two layers,

resulting in a fully sp^3-coordinated system with interior atoms sp^3-linked carbon atoms, and the external faces terminated with pyramidal nitrogen atoms (see Fig. 3).

Our results are shown in Fig. 3, where we can see three distinct regimes. Below ~10% nitrogen, no cross-linking between the layers occurs, and the system remains fully sp^2-coordinated. In the range 10–20% nitrogen the first interlayer C–C bonds form. Above 20–25% the cross-linking between carbon atoms in adjacent layers increases significantly, and the layered sp^2-carbon structure breaks down until, at 50% nitrogen, all the carbon atoms are sp^3-coordinated. Thus, these findings could also explain the different morphologies existing in N-doped MWNTs, which, as mentioned above, are associated with the different local amounts of N incorporated on these NTs.

Thus this result defines an upper limit for local substitutional nitrogen concentration in a sp^2-C layered system at around ~10–20%. At first sight this would appear a highly promising result, as it lies in a similar range as the upper doping limit observed in N-doped MWNTs.[44,45] It also coincides with the composition at which CN_x thin films have been shown to become ultra-hard,[46] whose TEM microstructures show heavily cross-linked layers and inter-layer spacings consistent with these calculated here. It is close to the threshold limit nitrogen concentration observed in N-implanted graphene,[27] and also matches early PM3 calculations of nitrogen-doped graphene monolayers which found sheet corrugation begins (corresponding to sp^2-C breakdown) at around 20% [N].[47]

However in fact, this predicted transition from sp^2-C towards sp^3-C at ~20% [N] is actually a misleading coincidence, as we will now show.

2.1 Nitrogen stabilisation of sp^2 carbon

Unfortunately the sp^2/sp^3 carbon ratio in nitrogen-doped carbon nanomaterials as a function of nitrogen concentration is rarely discussed, since typically the XPS C1s peaks are broad and difficult to deconvolute.[27] We therefore instead turn to

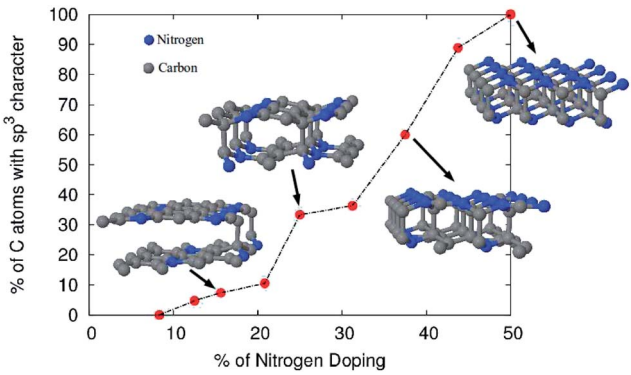

Fig. 3 Fraction of carbon atoms in sp^3 configuration in bilayer graphene as a function of substitutional nitrogen doping percentage, after full structural optimisation. sp^3 coordination in all cases consists of C–C cross-linking between layers. Ball and stick model structures of selected data points indicated by arrows are included.

the literature for nitrogen-doped tetrahedrally-amorphous carbon (ta-C). Previous theoretical works also indicated that N incorporation favors the formation of reactive C-sp^3 in adjacent sites.[48] Furthermore, this prediction has been also used to support the hypothesis that C-sp^3 atoms act as cross-linking sites.[46] However, experimentally it has been found that high nitrogen concentration CN_x films are composed of ~100% sp^2-configurations.[49,50] Fig. 4 shows two plots from different sample preparations. As can be seen, the predicted behavior here is the exact *inverse* of our finding above, namely, in the range 1–10% or 10–20% depending on the sample, the system undergoes a transition from primarily sp^3-coordinated carbon to sp^2-coordination, *i.e.* increasing the nitrogen concentration above this threshold appears to *stabilize* sp^2-coordination. We therefore need a different explanation of nitrogen behaviour at higher concentrations.

Our calculations thus far have assumed essentially homogenous samples with only substitutionally-bonded nitrogen bonding species. However as discussed above, XPS studies clearly see nitrogen in other configurations, notably pyridinic. This is the configuration shown in Fig. 2a, a nitrogen atom with only two neighbours, *i.e.* nitrogen adjacent to either an external or internal edge (such as vacancies).

Variable nitrogen concentration, [N], studies of these two peaks show the substitutional nitrogen 400.5 eV peak remains constant independent of [N], whereas the pyridinic 398.2 eV peak intensity is proportional to nitrogen concentration.[45] Studies of N-doped ultra-hard thin films grown by magnetron sputtering found a rapid increase in elastic recovery behaviour as [N] passed from 5 to 15%, with a corresponding rapid and continuous increase in the pyridinic 398 eV peak intensity as compared to the substitutional 400 eV peak.[52] Similar behavior was also seen in our recent X-ray photoelectron spectromicroscopy studies of the nitrogen ion implantation of nanotubes, where the pyridinic/substitutional ratio in randomly aligned multi-walled carbon nanotubes increased with [N].[53]

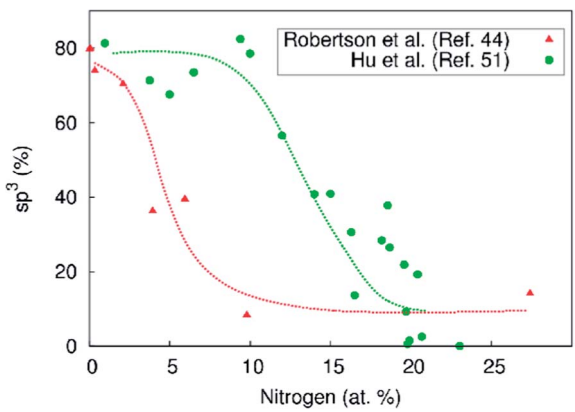

Fig. 4 sp^3-C fraction in nitrogen-doped tetrahedrally-amorphous carbon (ta-C) thin films as a function of nitrogen concentration as determined by EELS spectroscopy, showing a marked transition towards a high sp^2-fraction when the nitrogen concentration passes a threshold. Data from ref. 44 and 51. Data from ref. 51 is upshifted here by 10% as compared to that in the original reference, due to assumed mislabelling in the original published plot.

Similarly when implanting individual few-layer graphene sheets, we found that while the concentration of substitutional nitrogen increases by only about 1.6% between 5 and 15 min of nitrogen ion bombardment, the pyridinic concentration almost doubles from 2.5 to 4.7%.[27] Whilst these latter cases can be understood *via* the formation of carbon vacancies and voids due to the sputtering process, it would be desirable to see if there is a thermodynamic driving force towards pyridinic nitrogen formation at higher nitrogen concentrations. A way to achieve this would be through segregation, with primary possible segregation locations being edges (internal or external), grain boundaries, or new phase formation.

3 Nitrogen segregation at boundaries

Our calculations for a single substitutional nitrogen atom (N_{subst}) in a large 287 atom graphene sheet (0.3% N) show little change in bond length for the nitrogen compared to carbon, consistent with previous calculations[14,54] (shifts of less than 0.04 Å during geometrical optimisation after substitution). Our calculated formation enthalpy for substitutional nitrogen is +0.21 eV, using the formalism

$$E_F(N_{subst}) = E_{TOT} - n_c E_F(\text{graphene}) - 1/2 E_F(N_2) \quad (1)$$

where E_{TOT} is the total system energy for the nitrogen substituted graphene containing n_C carbon atoms, E_F(graphene) is the energy of one carbon atom in an infinite graphene sheet, $E_F(N_2)$ is the total energy for an N_2 molecule. By decreasing the hexagonal cell size we increase the nitrogen concentration while maintaining a homogenous nitrogen distribution. The trend in formation enthalpy is shown in Fig. 5; it can be seen that once a 2×2 8-atom cell is reached, the formation enthalpy for substitutional nitrogen has risen to +0.50 eV.

While this result precludes stabilization *via* simple nitrogen segregation to high density substitutional regions (at least, on the same sub-lattice), its primary

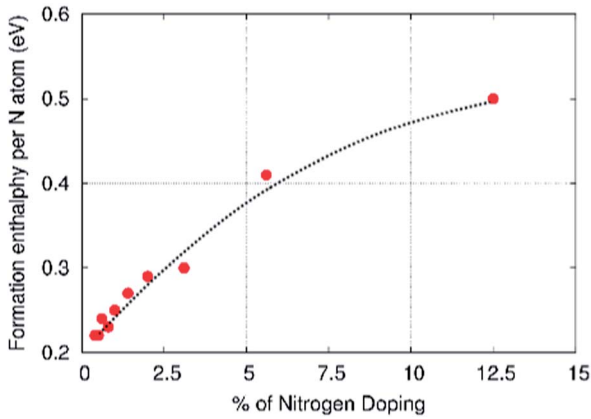

Fig. 5 Calculated formation enthalpy for homogeneously (hexagonally) distributed substitutional nitrogen in pristine infinite graphene, as a function of nitrogen concentration.

purpose is to provide formation enthalpies for comparison with alternative segregation routes.

There are three primary segregation possibilities for nitrogen in sp^2-carbon lattices: segregation *via* simple aggregation, segregation at boundaries (grain boundaries, sheet edges), and segregation *via* the formation of new phases. The first of these is effectively excluded above, so we next turn to segregation at sheet edges.

There are two primary cutting directions in the hexagonal graphene lattice, the $\langle 1\bar{1}00\rangle$ and the $\langle 2\bar{1}\bar{1}0\rangle$, creating so-called *armchair* and *zigzag*/*Klein* edges respectively. All intermediate orientations can be described in terms of alternating sections of these edge orientations,[55] in general called *chiral* edges. For a more detailed discussion of edge structure and termination see ref. 56.

In the following section we construct orthorhombic supercells with ~50 Å width graphene nanoribbons, since these have been shown to be sufficiently wide that the edges are decoupled.[56] Similar convergence criteria and cell dimensions are used to our previous studies with hydrogen,[56] hydroxyl,[57] sulphur and halogen[58] terminated edges, however we quote here formation enthalpies per nitrogen atom rather than per unit length to remain comparable to the bulk defect energies above.

In the case of nitrogen-terminated edges there are very few possible structural configurations, once nitrogen pairs and undercoordinated nitrogen atoms are excluded. We have considered here the two primary $\langle 1\bar{1}00\rangle$ and $\langle 2\bar{1}\bar{1}0\rangle$ edge structures, along with their formation enthalpies (Fig. 6). There are two key observations we draw, firstly that the armchair $\langle 1\bar{1}00\rangle$ edge structure is extremely unstable (E_F = +4.62 eV per nitrogen atom), and secondly the surprisingly high stability of the zigzag $\langle 2\bar{1}\bar{1}0\rangle$ edge structure (formation enthalpy of only +0.81 eV per N atom). Thus this result suggests that nitrogen-terminated edges are likely to be exclusively zigzag oriented.

Unfortunately, the few experimental works on this topic to date have investigated flat and homogeneous regions relatively far from the edge of the graphene layer.[23,26,28] However we note that this situation of exclusively nitrogen-terminated zigzag edges is in line with predictions and observations in h-BN.[60,61]

This result is also entirely consistent with the nitrogen-terminated vacancy shown in Fig. 2g. This is effectively the smallest possible zone of internal zigzag edge of the type discussed here, with three pyridinic nitrogen atoms surrounding a single carbon vacancy. Our calculated formation enthalpy for this defect in the centre of a very large 284 C atom supercell (*i.e.* at 1.0% [N]) is +0.80 eV per N atom, matching our low density edge value found here.

The +0.81 eV per N formation enthalpy for the zigzag edge shown above is close to the formation enthalpy for substitutional nitrogen in the 10–20% concentration range in the basal plane (+0.4 to +0.6 eV, see Fig. 5), but still remains higher. Thus simple segregation into zigzag nitrogen-terminated edges in this concentration range is not a candidate thermodynamic driving force for the observed behavioural change. However there are a number of ways that the formation enthalpy of such edges can be decreased further.

The first is to explore increasing effective edge density; in practice this could represent either a higher density of nitrogen terminated vacancy loops in the sheet, or increasingly small nitrogen-terminated polycyclic aromatic carbon patches (azacarbons). For our simulations we increase the edge site density by

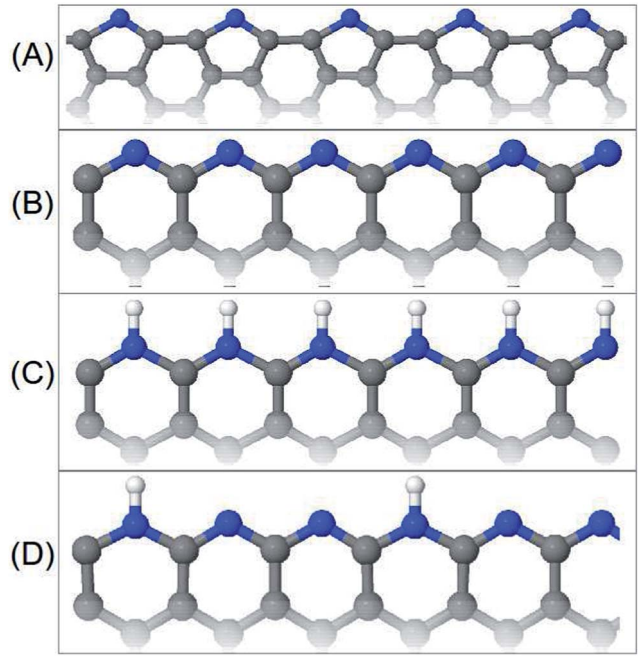

Fig. 6 Nitrogen-terminated edge structures (a) unstable $\langle 1\bar{1}00\rangle$ arm-chair structure (formation enthalpy of +4.62 eV per N), (b) stable $\langle 2\bar{1}\bar{1}0\rangle$ zigzag nitrogen-terminated edge (formation enthalpy of +0.81 eV per N), (c) fully hydrogenated $\langle 2\bar{1}\bar{1}0\rangle$ zigzag nitrogen-terminated edge (formation enthalpy of +0.23 eV per N), and significantly more stable than all of the others, (d) partially hydrogenated $\langle 2\bar{1}\bar{1}0\rangle$ zigzag nitrogen-terminated edge (formation enthalpy of −0.10 eV per N), a nitrogen analogue of the z_{211} hydrogenated zigzag edge.[59]

decreasing the width of nanoribbon we have simulated. The resulting variation in formation energy is shown in Fig. 7.

While decreasing the spacing between edges significantly decreases their formation enthalpy at high edge densities, at nitrogen concentrations in the 10–20% range the enthalpy decrease is relatively minor.

Another way to stabilize zigzag nitrogen-terminated edges is through interlayer interaction, for example if nitrogen-terminated azacarbons are attached to the surface of graphene or carbon nanotubes; preliminary calculations (not reported here) suggest this stabilizes such nitrogen-terminated edges significantly.

3.1 Hydrogen stabilisation of nitrogen-terminated edges

Finally we consider another novel way to further stabilize nitrogen-terminated zigzag edges, through modifying the edge chemistry. Noting that nitrogen is isoelectronic with (CH), we can draw analogies between nitrogen-terminated zigzag edges and hydrogenated zigzag edges.

DFT studies of hydrogen terminated zigzag edges demonstrated that the stability of single hydrogenated edges can be greatly increased by introducing an additional hydrogen to every third edge carbon atom. This converts the atom to sp^3 coordination and stabilizes the edge, opening up the band gap and removing the unstable dispersed Fermi level state that localizes along a singly hydrogenated

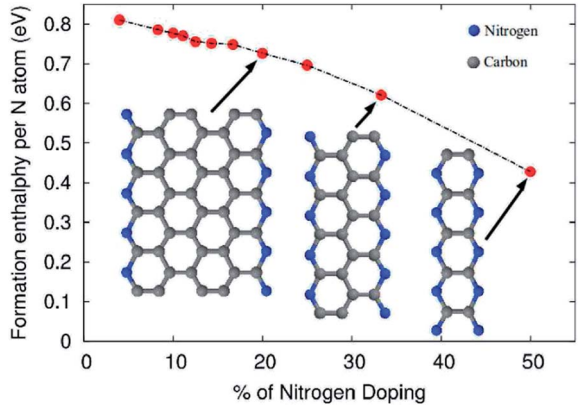

Fig. 7 Calculated effect of decreasing ribbon width on formation enthalpy of nitrogen terminated $\langle 2\bar{1}\bar{1}0\rangle$ zigzag edges in graphene. Formation enthalpy drops from +0.81 eV per N at [N] = 4% to +0.46 eV per N at [N] = 50%.

edge.[59] A similar effect was noted for the thermodynamically preferred reconstructed Klein edges.[56]

By analogy, hydrogenating every third nitrogen atom along a nitrogen-terminated zigzag edge should also stabilize that edge structure. We have tested this effect with the nitrogen edge-terminated graphene nanoribbons given in Fig. 7, both with a fully hydrogenated $(NH)_3$ edge, and with every third nitrogen hydrogenated $N_2(NH)$. The results are shown with filled circles in Fig. 8. The stabilizing effect on the edges is remarkable, dropping the formation energies at even low edge concentrations.

Just as for the hydrogenated carbon edge, the greatest stabilization comes from hydrogenating every third nitrogen atom, which goes so far as to render the formation enthalpy of the edge negative. Unlike the hydrogenated edge,[56] there is still significant stabilization upon total hydrogenation of the nitrogen edge. For the isolated edges at low % N, the formation enthalpy per N atom drops from +0.79 eV per N to +0.23 eV per N for the fully hydrogenated edge, and −0.10 eV per N for the edge with every third nitrogen hydrogenated. These formation energies mean that the binding enthalpy of $1/2H_2$ to an unfunctionalised zigzag nitrogen-terminated edge is a massive 2.67 eV, *i.e.* the unfunctionalised nitrogen zigzag edge will be highly chemically reactive.

While the formation enthalpies of these edge structures are now comparable and lower than those for substitutional nitrogen, a better measure in the presence of hydrogen is obtained by considering a molecular hydrogen gas atmosphere around the graphene edge. The calculated total edge formation energy E_{edge} can be adjusted using the hydrogen chemical potential μ_{H_2} and the hydrogen edge density ρ_H, to give a first approximation to the relative Gibb's free energy of the edge, G_{edge},

$$G_{edge} = E_{edge} - \rho_H \mu_{H_2}/2. \quad (2)$$

The hydrogen chemical potential μ_{H_2} depends on the pressure and temperature of the system.[59] As an indication, at ambient conditions the chemical

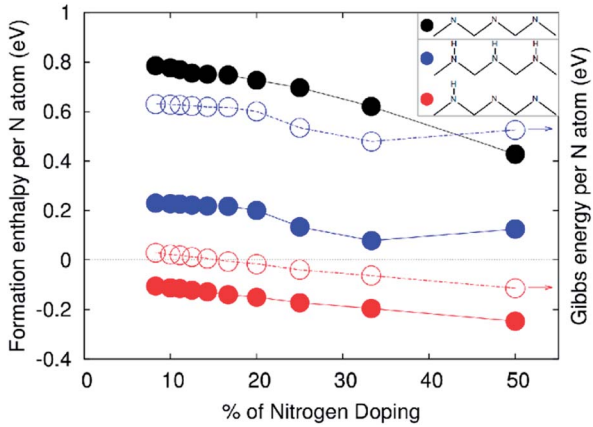

Fig. 8 Effect of total $(NH)_3$ (blue) and partial ($N_2(NH)$) (red) hydrogenation on the stability of nitrogen terminated $\langle 2\bar{1}\bar{1}0\rangle$ zigzag edges in graphene (for edge structures see Fig. 6C and D respectively). The formation enthalpy of pure N edges (black filled circles) is included for comparison. Formation enthalpies (filled circles) and Gibbs free energies (empty circles) are shown. A chemical potential of 0.8 eV is used for H_2 when calculating the Gibbs energies (see text).

potential μ_{H_2} at 300 K and partial H_2 pressure in air of $P_{H_2} \approx 10^{-4}$ mbar gives $\mu_{H_2} \approx -0.4$ eV.[62] For both decreasing P_{H_2} and increasing temperatures, the chemical potential decreases. Low temperature and higher pressure conditions ($\mu_{H_2} \approx -1.2$ to -0.5 eV) are currently of interest for cost efficient CVD graphene growth on metal surfaces.[63–66] In Fig. 8 the empty circles indicate the Gibbs free energy of formation for the fully and partially hydrogenated nitrogen zigzag edges, taking a typical hydrogen chemical potential of -0.8 eV.

This shows that the different nitrogen terminated zigzag edges, from non- to fully hydrogenated, span a similar energy range to the formation enthalpy for substitutional nitrogen at varying densities.

Clearly there are further terms that should be incorporated into the Gibb's free energy (such as edge entropy), and it is difficult to extrapolate a general argument much further than this, since thereafter experimental specifics such as growth conditions and gas atmosphere become predominant. However broadly, these edge results confirm our hypothesis that as nitrogen concentration increases in sp^2-nanocarbon samples, there should be a thermodynamic transition in stability between substitutional nitrogen, in favour of segregation to nitrogen terminated zigzag edges, almost certainly with some degree of heteroatom functionalisation. In sp^3-like ta-C, this effect will tend to favour the formation of nitrogen-terminated regions of sp^2-C, favouring a transition from sp^3 to sp^2 as observed. The formation energies of the hydrogenated nitrogen-terminated edges are in the right range. Notably, if feed gas chemical potential is important in determining the precise concentration at which this stability transition between substitutional and edge nitrogen occurs, this may also help to explain the different nitrogen concentrations in Fig. 4 at which the ta-C undergoes transition from sp^3 to sp^2, if this is dependent on the growth conditions.

4 Discussion

To summarise thus far, the calculations suggest that substitutional nitrogen should only be stable in sp^2 carbon layers at relatively low concentrations. At high concentrations (~15–20% and above) the presence of the nitrogen would cause the collapse of the π-cloud and breakdown of the sp^2 network *via* sp^3-cross linking between layers. However before this occurs, at intermediate concentrations (5–15%) it becomes thermodynamically favoured for nitrogen to segregate to nitrogen-terminated zigzag edges, for example at edges of sp^2-C patches or around holes in sp^2-C sheets. We emphasise that this is a relatively general thermodynamic analysis aimed at identifying trends in driving forces and thermodynamic concentration limits. Clearly experimental growth and dynamic implantation studies require additional input on the reaction kinetics and external environmental factors.

The model fits well with our recent HRTEM/EELS observations of nitrogen-doped single-walled carbon nanotubes (SWNTs)[24] (see Fig. 9). Bulk to nanometer-resolved EELS measurements of nitrogen-doped SWNTs typically show a pyramidal N1s spectra centred around 407 eV, resembling Fig. 9C(i and ii).[30,67] EELS simulations suggest that this signal comes from the σ* response of pyridinic nitrogen atoms,[24] and spatially mapping the EELS signal shows this signal comes primarily from amorphous and disordered regions in the sample, and amorphous material on the nanotube surfaces. In fact, atomic resolution EELS studies of pristine tube surfaces find very low nitrogen concentrations (typically much less than 1%), and EELS spectra of individual substitutional defects shows a very different spectral form (Fig. 9C(iii and iv)). In these cases there is a large, sharper peak centred around 400–403 eV, also ascribed primarily to σ* bonding, but of substitutional nitrogen. The observed peak splitting in Fig. 9C(iii) is explained *via* local lattice asymmetry in the σ bonds when the substitutional nitrogen sits next to a lattice defect such as in Fig. 9E.[24]

Thus in the case of nitrogen-doped SWNTs it appears that the non-local (down to nanometer-resolved) spectroscopic picture of nitrogen behavior is misleading and does not represent nitrogen incorporation in the nanotube itself. Instead the HRTEM, EELS and modeling results point towards a picture whereby nitrogen-doped SWNTs have very low concentrations of substitutional nitrogen doping. Thereafter the nitrogen level in the sample is increased *via* the presence of pyridinic nitrogen in the surface material attached to the tube, likely in the form of nitrogen-terminated zigzag edges of polycyclic carbon patches.

This strongly resembles the behavior of oxygen impurities and associated functionalisation for single-walled[68] and multi-walled nanotubes,[69–72] carbon fibres,[73] and graphene oxide.[74–76] These studies demonstrate that many of the observed oxygen-derived functional groups previously assigned to these nanocarbon objects are actually associated with oxidative debris; highly oxidized polycyclic aromatic carbon patches attached to the surface of the nanobject, which can often be removed *via* base washing, an approach which would be interesting to try with the nitrogen-doped samples. In the case of graphene oxide it has been shown that the oxidative debris is inherently electroactive, and may in fact account for the majority of the electroactivity which makes graphene oxide an interesting material for energy storage applications such as supercapacitors.[76] It

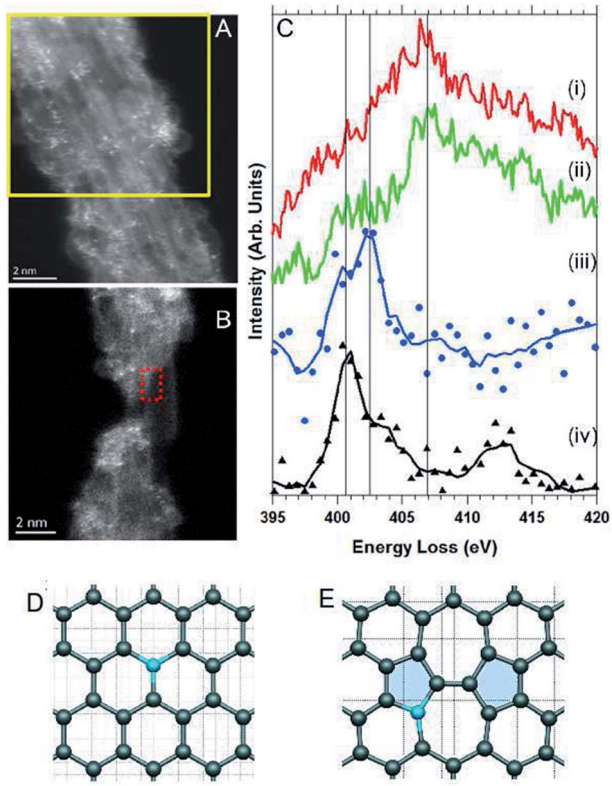

Fig. 9 Spatially-resolved EELS from nitrogen containing SWNTs and associated debris. (A) and (B) HAADF images of a bundle of single-walled nanotubes covered by an amorphous material. (C) N1s ELNES spectra obtained from (i) a cumulative EELS spectrum over the area in A marked by the yellow rectangle, (ii) sum of 10 spatially localised EELS spectra from the top-left corner of the red dotted rectangle in B. (i) and (ii) correspond to typical 'bulk' EELS spectra for nitrogen-doped SWNTs. In contrast, (iii) shows the spectrum obtained from a single pixel (non-averaged) at a substitutional nitrogen atom in the wall of a SWNT as shown in D, and (iv) a similar spectrum from substitutional nitrogen neighbouring a topological defect, as shown in E ("pyrrolic" N). These local substitutional defects clearly show a markedly different peak profile to the bulk measurements, in agreement with our proposition that the majority of nitrogen in the sample is not embedded in the nanotube wall but is instead in the intervening "amorphous" material. (Figure adapted from ref. 24.)

seems possible that the enhanced supercapacitive performance seen for nitrogen-doped nanotubes[5,7,16,17,77,78] for example, may also be strongly affected by the presence of nitrogen-terminated polycyclic fragments attached to the material surface.

There are also structural implications for the morphology of heavily nitrogen-doped MWNTs. Addition of nitrogen to the feedstock gas in CVD nanotube growth modifies the classic MWNT geometry, from walls aligned parallel to the nanotube axis to either a compartmentalised structure ('bamboo' nanotubes), or a structure where the nanotube walls are inclined at a fixed angle to the nanotube axis ('herringbone' nanotubes), similar to a series of stacked cones (with or without a hollow core, see Fig. 10). This second structure has potentially very different physical and chemical behavior to conventional parallel wall tubes, not

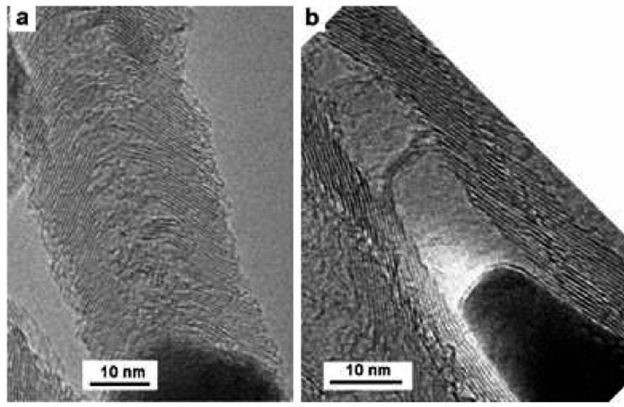

Fig. 10 HRTEM showing typical stacked-cup structure of nitrogen-doped herringbone multi-walled carbon nanotubes (figure from ref. 79).

least in terms of surface activity. Whereas conventional tubes surface terminate with a graphene basal plane, the graphene planes in herringbone tubes terminate at the tube surface, and therefore (excepting the case of layer folding) the nanotube surface consists of basal plane edges. Our current results suggest a mechanism of nitrogen stabilization of edge sites and may be relevant in the structural stability and subsequent surface chemistry of herringbone tubes.

The current article has focused on the interplay between substitutional and pyridinic-type nitrogen. The chemistry of the nitrogen–carbon system is more complex and richer than this, for example we have not considered here the capability of nitrogen to stabilize regions of high curvature within an sp^2-carbon lattice *via* the formation of pentagons[46,52] and pentagon pairs,[80] or the interaction between nitrogen and carbon nanomaterial catalysts, and resultant effects on the growth kinetics and subsequent morphology. Nonetheless we hope to have identified some key general points in nitrogen behaviour in nanocarbons. The first of these is the general observation of a thermodynamic driving force towards segregation at $\langle 2\bar{1}\bar{1}0\rangle$ zigzag edges in sp^2-C networks above a certain nitrogen concentration, resulting in N-edge terminated PAHs and hole formation, and stabilising N-edge terminated sp^2 material in nitrogen-doped carbon thin films. The second is that much of the nitrogen observed in 'N-doped' nanocarbons may instead be present in amorphous and polycyclic carbon species attached to the nanocarbon surface, notably as pyridinic nitrogen at edge sites in such material. This attached material may be responsible for some of the improved electroactive behaviour observed in nitrogen-doped nanocarbons. We have also tried to highlight the complementarity between atomically resolved EELS, time resolved XPS and DFT calculations, in unravelling the complex and fascinating interactions between nitrogen and carbon.

5 Computational method

Spin polarized density functional (DFT) calculations using LDA-PW92 (ref. 81) were performed as implemented in the AIMPRO code.[82–84] The calculations were carried out using supercells, fitting the charge density to plane waves with an energy cutoff of 150 Hartrees. Relativistic pseudopotentials generated by

Hartwigsen, Goedecker and Hutter were used.[85] 22 and 40 independent Gaussian functions were used as basis sets for carbon and nitrogen respectively, 12 for hydrogen. Periodic boundary conditions have been applied by using supercells. Supercell sizes have been checked and chosen to be sufficiently large (vacuum distance between all 1-D and 2-D structures larger than 15 Å) to avoid interactions. The bilayer graphene systems were arranged with AB stacking, with cells containing up to 64 atoms depending on system symmetry. A fine k-point grid was chosen (from $2 \times 2 \times 1$ to $8 \times 8 \times 1$ for bilayer graphene depending on cell size, $8 \times 1 \times 1$ for graphene nanoribbons), and electronic level occupation was obtained using a Fermi occupation function with $kT = 0.04$ eV. Absolute energies are converged in the self-consistency cycle to better than 10^{-5} Ha. Atomic positions and lattice parameters were geometrically optimized until the maximum atomic position change in a given iteration dropped below 10^{-4} a_0 (a_0: Bohr radius).

Acknowledgements

We would like to acknowledge TUBITAK-2219 Abroad Post-Doctoral Research Funding Programme (Ref. no. 1059B191301289) for supporting DE. CB and MS are supported by the Belgian Fund for Scientific Research (FSR-FNRS) under contract 'CHEMOGRAPHENE' (no. 2.4577.11). CPE, PW acknowledge the French SPRINT project ANR-10-BLAN-0819. RA acknowledges the European Union Seventh Framework Program under Grant Agreement 312483 – ESTEEM2 (Integrated Infrastructure Initiative – I3), and all authors the COST network MP0901 NanoTP. We thank Odile Stephan, Katia March, Matthieu Kociak and Annick Loiseau for stimulating discussions. CE and CB thank PHC Tournesol 31160RC for funding. R.A. acknowledges funding from the Spanish Ministerio de Economia y Competitividad (FIS2013-46159-C3-3-P).

References

1 Y. Ma, A. Foster, A. V. Krasheninnikov and R. Nieminen, *Phys. Rev. B: Condens. Matter Mater. Phys.*, 2005, **72**, 205416.
2 C. Zhou, J. Kong, E. Yenilmez and H. Dai, *Science*, 2000, **290**, 1552–1555.
3 Y. K. Yap, *B-C-N Nanotubes and Related Nanostructures*, Springer, 2009.
4 M. Monthioux, *Introduction, Carbon Meta-Nanotubes: Synthesis, Properties and Applications*, John Wiley & Sons, 2011.
5 P. Ayala, R. Arenal, A. Loiseau, A. Rubio and T. Pichler, *Rev. Mod. Phys.*, 2010, **82**, 1843–1885.
6 Q. Jiao, L. Hao and Y. Zhao, *Carbon*, 2013, **61**, 647–649.
7 C. P. Ewels and M. Glerup, *J. Nanosci. Nanotechnol.*, 2005, **5**, 1345.
8 P. Ayala, R. Arenal, M. Rummeli, A. Rubio and T. Pichler, *Carbon*, 2010, **48**, 575–586.
9 H. R. Barzegar, E. Gracia-espino, T. Shari, F. Nitze and T. Wagberg, *J. Phys. Chem. C*, 2013, **117**, 25805–25816.
10 A. Lopez-Bezanilla, *J. Phys. Chem. C*, 2014, **118**, 1472–1477.
11 A. P. Alegaonkar, A. Kumar, S. H. Patil, K. R. Patil, S. K. Pardeshi and P. S. Alegaonkar, *J. Phys. Chem. C*, 2013, **117**(51), 27105–27113.

12 M. A. Kanygin, O. V. Sedelnikova, I. P. Asanov, L. G. Bulusheva, A. V. Okotrub, P. P. Kuzhir, A. O. Plyushch, S. A. Maksimenko, K. N. Lapko, A. A. Sokol, O. A. Ivashkevich and P. Lambin, *J. Appl. Phys.*, 2013, **113**, 144315.
13 V. Krstic, G. L. J. A. Rikken, P. Bernier, S. Roth and M. Glerup, *Europhys. Lett.*, 2007, **77**, 37001.
14 A. Zhao, J. Masa, W. Schuhmann and W. Xia, *J. Phys. Chem. C*, 2013, **117**, 2428324291.
15 Y. Tang, S. C. Burkert, Y. Zhao, W. A. Saidi and A. Star, *J. Phys. Chem. C*, 2013, **117**, 25213–25221.
16 R. Mi, H. Liu, H. Wang, K.-W. Wong, J. Mei, Y. Chen, W.-M. Lau and H. Yan, *Carbon*, 2014, **67**, 744–752.
17 S. Hussain, R. Amade, E. Jover and E. Bertran, *J. Mater. Sci.*, 2013, **48**, 7620–7628.
18 J.-J. Adjizian, R. Leghrib, A. A. Koos, I. Suarez-Martinez, A. Crossley, P. Wagner, N. Grobert, E. Llobet and C. P. Ewels, *Carbon*, 2014, **66**, 662–673.
19 Q. Sheng, R. Liu and J. Zheng, *Bioelectrochemistry*, 2013, **94**, 39–46.
20 C. Shan, W. Zhao, X. L. Lu, D. J. O'Brien, Y. Li, Z. Cao, A. L. Elias, R. Cruz-Silva, M. Terrones, B. Wei and J. Suhr, *Nano Lett.*, 2013, **13**, 5514–5520.
21 R. Droppa Jr, P. Hammer, A. C. M. Carvalho, M. C. dos Santos and F. Alvarez, *J. Non-Cryst. Solids*, 2002, **299**, 874–879.
22 M. Glerup, J. Steinmetz, D. Samaille, O. Stephan, S. Enouz, A. Loiseau, S. Roth and P. Bernier, *Chem. Phys. Lett.*, 2004, **387**, 193.
23 T. Susi, J. Kotakoski, R. Arenal, S. Kurasch, H. Jiang, V. Skakalova, O. Stephan, A. V. Krasheninnikov, E. I. Kauppinen, U. Kaiser, *et al.*, *ACS Nano*, 2012, **6**, 8837–8846.
24 R. Arenal, K. March, C. P. Ewels, X. Roquefelte, M. Kociak, A. Loiseau and O. Stephan, *Nano Lett.*, 2014, DOI: 10.1021/nl501645g.
25 C. J. Lee, S. C. Lyu, H.-W. Kim, J. H. Lee and K. I. Cho, *Chem. Phys. Lett.*, 2002, **359**, 115.
26 J. C. Meyer, S. Kurasch, H. J. Park, V. Skakalova, D. Knzel, A. Gro, A. Chuvilin, G. Algara-Siller, S. Roth, T. Iwasaki, U. Starke, J. H. Smet and U. Kaiser, *Nat. Mater.*, 2011, **10**, 209–215.
27 M. Scardamaglia, B. Aleman, M. Amati, C. Ewels, P. Pochet, N. Reckinger, J. F. Colomer, T. Skaltsas, N. Tagmatarchis, R. Synders, L. Gregoratti and C. Bittencourt, *Carbon*, 2014, **73**, 371.
28 U. Bangert, W. Pierce, D. M. Kepaptsoglou, Q. Ramasse, R. Zan, M. H. Gass, J. A. Van den Berg, C. B. Boothroyd, J. Amani and H. Hofsass, *Nano Lett.*, 2013, **13**, 4902–4907.
29 D. Marton, K. J. Boyd, A. H. al Bayati, S. S. Todorov and J. W. Rabalais, *Phys. Rev. Lett.*, 1994, **73**(1), 118.
30 H. Lin, R. Arenal, S. Enouz-Vedrenne, O. Stephan and A. Loiseau, *J. Phys. Chem. C*, 2009, **113**, 9509–9511.
31 R. Arenal, O. Stephan, P. Bruno and D. M. Gruen, *Appl. Phys. Lett.*, 2009, **94**, 111905.
32 H. Wang, T. Maiyalagan and X. Wang, *ACS Catal.*, 2012, **2**, 781–794.
33 J. Casanovas, J. M. Ricart, J. Rubio, F. Illas and J. M. Jime, *J. Am. Chem. Soc.*, 1996, **7863**, 8071–8076.
34 J. M. Ripalda, E. Roman, N. Diaz, L. Galan, I. Montero, G. Comelli, A. Baraldi, S. Lizzit, A. Goldoni and G. Paolucci, *Phys. Rev. B: Condens. Matter Mater. Phys.*, 1999, **60**, 3705–3708.

35 I. Shimoyama, G. Wu, T. Sekiguchi and Y. Baba, *Phys. Rev. B: Condens. Matter Mater. Phys.*, 2000, **62**, 6053–6056.
36 C. Ronning, H. Feldermann, R. Merk, H. Hofsass, P. Reinke and J. U. Thiele, *Phys. Rev. B: Condens. Matter Mater. Phys.*, 1998, **58**(4), 2207.
37 A. Jorio, M. S. Dresselhaus, R. Saito and G. Dresselhaus, *Raman Spectroscopy in Graphene Related Systems*, Wiley-VCH Verlag, 2011.
38 E. S. Reich, C. Thomsen and J. Maultzsch, *Carbon Nanotubes: Basic Concepts and Physical Properties*, Wiley-VCH, 2004.
39 I. Maciel, N. Anderson, M. Pimenta, A. Hartschuh, H. Quian, M. Terrones, H. Terrones, J. Campos-Delgado, A. Rao, L. Novotny and A. Jorio, *Meteorit. Planet. Sci.*, 2008, **7**, 878.
40 F. Villalpando-Paez, A. Zamudio, A. Elias, H. Son, E. Barros, S. Chou, Y. Kim, H. Muramatsu, T. Hayashi, J. Kong, H. Terrones, G. Dresselhaus, M. Endo, M. Terrones and M. Dresselhaus, *Chem. Phys. Lett.*, 2006, **424**, 345–352.
41 M. Glerup, M. Castignolles, M. Holzinger, G. Hug, A. Loiseau and P. Bernier, *Chem. Commun.*, 2003, 2542.
42 I. Florea, O. Ersen, R. Arenal, D. Ihiawakrim, C. Messaoudi, K. Chizari, I. Janowska and C. Pham-Huu, *J. Am. Chem. Soc.*, 2012, **134**, 9672–9680.
43 M. Castignolles, Ph.D. thesis, Universit Montpellier II, France, 2004.
44 J. Robertson and C. A. Davis, *Diamond Relat. Mater.*, 1995, **4**, 441–444.
45 S. Souto, M. Pickholz, M. C. dos Santos and F. Alvarez, *Phys. Rev. B: Condens. Matter Mater. Phys.*, 1998, **57**(4), 2536.
46 H. Sjöström, S. Stafström, M. Boman and J.-E. Sundgren, *Phys. Rev. Lett.*, 1995, **75**, 1336–1339.
47 M. dos Santos and F. Albarez, *Phys. Rev. B: Condens. Matter Mater. Phys.*, 1998, **58**, 13918.
48 S. Stafstrom, *Appl. Phys. Lett.*, 2000, **77**, 3941–3943.
49 W. J. Gammon, D. I. Malyarenjo, O. Kraft, G. L. Hoatson, A. C. Reilly and B. C. Holloway, *Phys. Rev. B: Condens. Matter Mater. Phys.*, 2002, **66**, 153402.
50 W. J. Gammon, G. L. Hoatson, B. C. Holloway, R. L. Vold and A. C. Reilly, *Phys. Rev. B: Condens. Matter Mater. Phys.*, 2003, **68**, 195401.
51 J. Hu, P. Yang and C. M. Lieber, *Phys. Rev. B: Condens. Matter Mater. Phys.*, 1998, **57**, R3185.
52 N. Hellgren, M. Johansson, E. Broitman, L. Hultman and J.-E. Sundgren, *Phys. Rev. B: Condens. Matter Mater. Phys.*, 1999, **59**, 5162.
53 M. Scardamaglia, M. Amati, B. Llorente, P. Mudimela, J.-F. Colomer, J. Ghijsen, C. Ewels, R. Snyders, L. Gregoratti and C. Bittencourt, *Carbon*, 2014, **77**, 319–328.
54 J.-Y. Yi and J. Bernholc, *Phys. Rev. B: Condens. Matter Mater. Phys.*, 1993, **47**, 1708–1711.
55 P. S. Branicio, M. H. Jhon, C. K. Gan and D. J. Srolovitz, *Modell. Simul. Mater. Sci. Eng.*, 2011, **19**, 054002.
56 P. Wagner, V. V. Ivanovskaya, M. Melle-Franco, B. Humbert, J.-J. Adjizian, P. R. Briddon and C. P. Ewels, *Phys. Rev. B: Condens. Matter Mater. Phys.*, 2013, **88**, 094106.
57 P. Wagner, C. P. Ewels, V. V. Ivanovskaya, P. R. Briddon, A. Pateau and B. Humbert, *Phys. Rev. B: Condens. Matter Mater. Phys.*, 2011, **84**, 134110.

58 P. Wagner, C. P. Ewels, J.-J. Adjizian, L. Magaud, P. Pochet, S. Roche, A. Lopez-Bezanilla, V. V. Ivanovskaya, A. Yaya, M. Rayson, P. Briddon and B. Humbert, *J. Phys. Chem. C*, 2013, **117**, 26790–26796.
59 T. Wassmann, A. P. Seitsonen, A. M. Saitta, M. Lazzeri and F. Mauri, *Phys. Rev. Lett.*, 2008, **101**, 096402.
60 C. Jin, F. Lin, K. Suenaga and S. Iijima, *Phys. Rev. Lett.*, 2009, **102**, 195505.
61 E. Machado-Charry, P. Boulanger, L. Genovese, N. Mousseau and P. Pochet, *Appl. Phys. Lett.*, 2012, **101**, 132405.
62 M. W. Chase, *J. Phys. Chem. Ref. Data*, 1998, **9**, 1–1951.
63 X. Li, W. Cai, J. An, S. Kim, J. Nah, D. Yang, R. Piner, A. Velamakanni, I. Jung, E. Tutuc, S. K. Banerjee, L. Colombo and R. S. Ruoff, *Science*, 2009, **324**, 1312–1314.
64 L. Gao, W. Ren, J. Zhao, L.-P. Ma, Z. Chen and H.-M. Cheng, *Appl. Phys. Lett.*, 2010, **97**, 183109.
65 K. Celebi, M. T. Cole, K. B. K. Teo and H. G. Park, *Electrochem. Solid-State Lett.*, 2011, **15**, K1–K4.
66 A. T. Murdock, A. Koos, T. B. Britton, L. Houben, T. Batten, T. Zhang, A. J. Wilkinson, R. E. Dunin-Borkowski, C. E. Lekka and N. Grobert, *ACS Nano*, 2013, **7**, 1351–1359.
67 S. Enouz-Vdrenne, O. Stphan, M. Glerup, J.-L. Cochon, C. Colliex and A. Loiseau, *J. Phys. Chem. C*, 2008, **112**, 16422–16430.
68 L. Shao, G. Tobias, C. G. Salzmann, B. Ballesteros, S. Y. Hong, A. Crossley, B. G. Davis and M. L. H. Green, *Chem. Commun.*, 2007, 5090–5092.
69 R. Verdejo, S. Lamoriniere, B. Cottam, A. Bismarck and M. Shaffer, *Chem. Commun.*, 2007, 513–515.
70 S. Fogden, R. Verdejo, B. Cottam and M. Shaffer, *Chem. Phys. Lett.*, 2008, **460**, 162–167.
71 C. Salzmann, S. Llewellyn, G. Tobias, M. Ward, Y. Huh and M. Green, *Adv. Mater.*, 2007, **19**, 883–887.
72 Z. Wang, M. D. Shirley, S. T. Meikle, R. L. Whitby and S. V. Mikhalovsky, *Carbon*, 2009, **47**, 73–79.
73 Z. Wu, C. U. Pittman Jr and S. D. Gardner, *Carbon*, 1995, **33**, 597–605.
74 J. P. Rourke, P. A. Pandey, J. J. Moore, M. Bates, I. A. Kinloch, R. J. Young and N. R. Wilson, *Angew. Chem., Int. Ed.*, 2011, **50**, 3173–3177.
75 A. F. Faria, D. S. T. Martinez, A. C. M. Moraes, M. E. H. Maia da Costa, E. B. Barros, A. G. Souza Filho, A. J. Paula and O. L. Alves, *Chem. Mater.*, 2012, **24**, 4080–4087.
76 A. Bonanni, A. Ambrosi, C. K. Chua and M. Pumera, *ACS Nano*, 2014, **8**, 4197–4204.
77 L. G. Bulusheva, E. O. Fedorovskaya, A. G. Kurenya and A. V. Okotrub, *Phys. Status Solidi B*, 2013, **250**, 2586–2591.
78 R. A. Fisher, M. R. Watt and W. Jud Ready, *ECS J. Solid State Sci. Technol.*, 2013, **2**, M3170–M3177.
79 M. Monthioux, L. Noe, L. Dussault, J.-C. Dupin, N. Latorre, T. Ubieto, E. Romeo, C. Royo, A. Monzon and C. Guimon, *J. Mater. Chem.*, 2007, **17**, 4611–4618.
80 C. Ewels, *Nano Lett.*, 2006, **6**, 890–895.
81 J. Perdew and P. Wang, *Phys. Rev. B: Condens. Matter Mater. Phys.*, 1992, **45**, 13244–13249.

82 P. R. Briddon and R. Jones, *Phys. Status Solidi B*, 2000, **217**, 131–171.
83 M. J. Rayson and P. R. Briddon, *Phys. Rev. B: Condens. Matter Mater. Phys.*, 2009, **80**, 205104.
84 P. R. Briddon and M. J. Rayson, *Phys. Status Solidi B*, 2011, **248**, 1309–1318.
85 C. Hartwigsen, S. Goedecker and J. Hutter, *Phys. Rev. B: Condens. Matter Mater. Phys.*, 1998, **58**, 3641.

